

Magnetization rotation in a superconductor/ferromagnet bilayer ring structure

Diana G. Gheorghe and Rinke J. Wijngaarden

Department of Physics and Astronomy, Faculty of Sciences, Vrije Universiteit, De Boelelaan 1081, 1081 HV Amsterdam, The Netherlands

Christopher Bell and Jan Aarts

Magnetic and Superconducting Materials Group, Kamerlingh Onnes Laboratory, University Leiden, P.O. Box 9504, 2300 RA Leiden, The Netherlands

(Received 21 June 2009; revised manuscript received 6 September 2009; published 16 October 2009)

The magnetic-flux distribution in a bilayer ring consisting of superconducting Nb and ferromagnetic amorphous Gd₁₉Ni₈₁ is studied at low temperature by magneto-optical imaging. The ring is macroscopic with an outer diameter of 500 μm and an inner diameter of 300 μm . Below the superconducting transition and with a small magnetic field applied along the ring axis, we observe a field enhancement at the inner edge and a field reduction at the outer edge, opposite to what is observed for a bare superconducting ring. With help from numerical simulations we show this to be due to an in-plane rotation of the magnetization of the Gd₁₉Ni₈₁ layer toward the radial direction, under the influence of shielding currents in the superconductor. In the superconductor, the resulting stray field of the magnetic layer is in the same direction as the field due to the superconducting shielding currents. As a consequence, these shielding currents are reduced. Alternatively, for a fixed critical current, the superconductor will be able to withstand a larger external field if coated by the magnetic material; it is hardened by it.

DOI: [10.1103/PhysRevB.80.144518](https://doi.org/10.1103/PhysRevB.80.144518)

PACS number(s): 74.78.-w, 75.25.+z, 75.70.-i, 74.25.Sv

I. INTRODUCTION

Despite their antagonistic character, the interplay between superconductivity (S) and ferromagnetism (F) may well lead to synergy, in a number of different ways. In thin-film S/F hybrids there can either be effects related to the exchange interaction (present in the F layer) on Cooper pairs close to the S/F interface or of electromagnetic interactions between S and F layers. Exchange interactions lead to pair breaking, thereby lowering the pair density on the S side of the interface. This is a form of the proximity effect. They also affect the superconducting correlations induced on the F side, which can lead to phenomena such as π junctions and triplet pairing.^{1,2} On the S side of the S/F interface, the sampling of inhomogeneous exchange fields by the Cooper pair leads to enhanced superconductivity as compared to the effect of a homogeneous exchange field.³ The effects of electromagnetic interactions are even more numerous. Stray fields from the ferromagnet directly affect the superconductor. Two somewhat nontrivial examples of this are the use of stray-field control of a supercurrent by rotating the magnetization in a small ferromagnetic block on top of a superconducting bridge⁴ and the variations in the superconducting transition temperature in F/S/F trilayers when the magnetization direction in the F layers is changed from parallel to antiparallel.^{5,6} Stray fields can also compensate an external field, which was used to induce superconductivity above the domain wall of an insulating ferromagnet⁷ or in S/F multilayers with perpendicular magnetization.⁸

It should also be possible to improve, rather than simply affect, the properties of the superconductor. In a recent series of theoretical papers,^{9,10} the shielding of superconducting strips and rings with soft magnetic materials was proposed as a method to increase their dissipation-free transport and to minimize ac losses. Basically, a suitable magnetic environ-

ment can lead to a reduction of the self-fields and consequently to a hardening of the superconductors and an increase of their critical currents. These theoretical predictions were verified experimentally for superconducting wires coated with soft magnetic materials¹¹ and for thin films placed in close contact with soft magnetic materials.^{12,13}

Less investigated is the effect which the superconductor can have on the magnetic state of the magnet. Magnetization measurements using a microfabricated Hall probe on Al/Ni submicron samples showed that shielding currents can reshuffle magnetic domains.¹⁴ Similarly, magnetization measurements by superconducting quantum interference device magnetometry on S/F multilayers demonstrated changes in the magnetic state of the F layers in response to the onset of superconductivity.^{15,16}

In this work we follow a different approach to study the effects of superconducting shielding currents on the distribution of the magnetization and vice versa. We use magneto-optical imaging to measure the z component of the magnetic field just above an S/F bilayer ring structure, to have well-defined shielding currents. Furthermore, we use an amorphous magnet with almost negligible coercive field so that the effect of domain-wall pinning on the reorientation of the magnetization is virtually negligible.

The data are compared with the outcome of numerical simulations, which allow to extract the separate responses of the magnet and of the superconductor from the experiment. We find that the “self-field” due to the shielding currents in the superconducting layer rotates the magnetization of the magnetic layer from its initial tangential direction toward the radial direction of the ring. In the superconductor, the resulting stray field of the magnetic layer is in the same direction as the self-field; the stray field and the self-field together shield the superconductor from the applied magnetic field. As a consequence, to maintain the same shielding in the

presence of the magnetic layer, both the self-field and the shielding currents flowing in the superconductor are reduced. Alternatively, with the same critical current, the superconductor will be able to withstand a larger external field if coated by the magnetic material; the superconductor is hardened against (perpendicularly) applied magnetic fields.

II. SAMPLE PREPARATION AND EXPERIMENTAL RESULTS

The sample was deposited on a Si(100) substrate in a two-step process at room temperature. First, a 40 nm Nb film was grown by dc magnetron sputtering in a ultrahigh vacuum system with base pressure $<2 \times 10^{-9}$ mbar. Following this, a 75 nm amorphous (denoted a-) $\text{Gd}_{19}\text{Ni}_{81}$ film was rf sputtered in a vacuum system with a base pressure below 2×10^{-6} mbar. Deposition rates were of the order of ~ 7.2 nm/min for the Nb and ~ 7.5 nm/min for the a- $\text{Gd}_{19}\text{Ni}_{81}$, as calibrated from low-angle x-ray reflectivity. The composite film was patterned with electron-beam lithography followed by broad beam Ar-ion etching to form ring structures with inner and outer diameters of 300 and 500 μm , respectively. A schematic view of the sample is given in Fig. 1(a). The properties of the superconducting and the ferromagnetic film have been reported before.^{17,18} Typical values for the sputtered Nb films are a superconducting transition temperature of 9.0 K, a zero-temperature Ginzburg-Landau coherence length $\xi_{GL}(0)$ of 12 nm, and a zero-temperature depairing current density of 1.6×10^{12} A/m².¹⁷ The transition temperature of the Nb/a- $\text{Gd}_{19}\text{Ni}_{81}$ sandwich was not measured with great precision but is in the range of 6–7 K. The difference with the single Nb film stems from the proximity effect which suppresses the order parameter in the Nb. The value for $\xi_{GL}(0)$ is considerably smaller than for pure Nb, which is due to the relatively small mean-free path (around 8 nm) of electrons in the sputtered films. This also affects the London penetration depth λ_L , which is estimated to be about 50 nm.¹⁷ The film is therefore a type-II superconductor, with a thickness of the order of the penetration depth, and the zero-temperature value of the lower critical field H_{c1} is approximately given by $\Phi_0/(4\pi\lambda_L^2) = 65$ mT. Taking $\lambda_L^2 \propto 1 - (T/T_c)^4$ this yields 50 mT at 4.2 K. In our experiments, the applied field is perpendicular to the thin-film surface. A rough estimate of the demagnetization factor may be obtained by approximating the ring with a strip of elliptic cross section. This yields for the field enhancement a factor $\frac{\pi w}{2d}$, where w is the width of the ring and d is its thickness. For a discussion see Ref. 19. For the present sample this means that the perpendicularly applied field is enhanced at the edge of the ring by a factor 4000. Using the value $H_{c1} = 50$ mT given above, the penetration field is only 12.5 μT . Hence in this experiment, vortices are always present in the sample, which is always in the mixed state.

In our magneto-optical imaging^{20–22} measurements, the sample was first cooled in zero applied field to $T = 3$ K, well below the critical temperature of the Nb film ($T_c \approx 7$ K), followed by an increase in the external magnetic field $\mu_0 H_{z,ext}$ from 0–3 mT with increments of 0.3 mT. After each

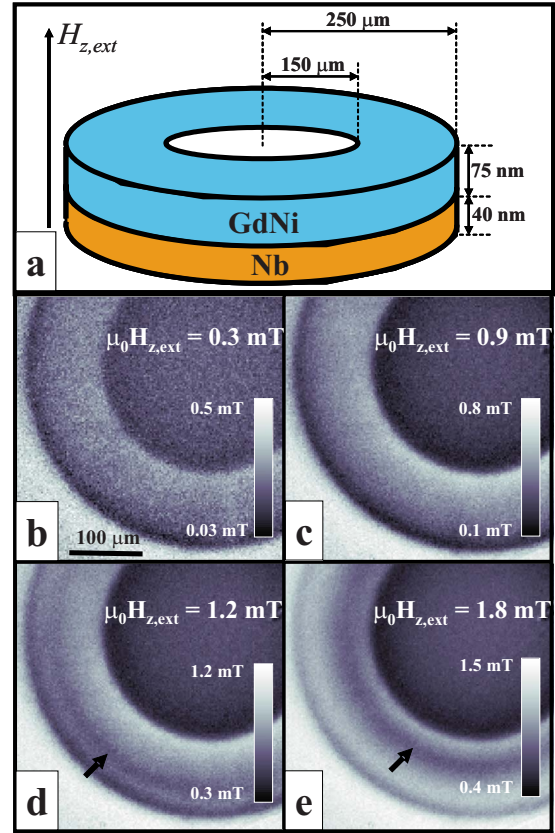


FIG. 1. (Color online) Schematic (not to scale) representation of the sample (a) and magneto-optical images [(b)–(e)] showing the evolution of the perpendicular component of the magnetic field at the surface of the sample, with increasing magnitude of the externally applied perpendicular field $H_{z,ext}$. The images were taken at $T = 3$ K. For clarity, the sample is not shown completely. The black arrow in figures (c) and (d) indicates the position of the dark ring at the surface of the sample. In the images, white regions indicate high local magnetic fields while black areas have small local fields, as defined by the scalebars.

increase in $H_{z,ext}$ a picture was taken using our magneto-optical polarization microscope setup.²¹ The local-field distribution was visualized with a Bi-doped yttrium iron garnet with a saturation field of 40 mT, placed in contact with the sample. This technique allows the direct visualization of the z component of the local magnetic field, i.e., the component perpendicular to the plane of the sample. In the images, high fields are bright and low fields are dark.

The evolution of the magnetization of the sample with increasing magnitude of the externally applied field $H_{z,ext}$ is not trivial. Prior to the application of the $H_{z,ext}$, the contour of the sample appears on an overall gray background. This is never observed for bare superconducting films and must be due to a small stray field from the magnetic layer. Upon increasing the applied field, a bright outline, corresponding to a strong local magnetic field that is parallel to the applied field, appears at the inner edge of the sample, Figs. 1(b) and 1(c) whereas its outer edge becomes dark, indicating a small magnetic field. This situation is exactly the opposite from what is observed for a superconducting ring without a magnetic layer,²³ where the local field is large (and parallel to the

applied field) at the outer edge and small at the inner edge.

As the applied magnetic field is increased, the bright and dark contours of the sample become more pronounced as a result of the enhancement of the local magnetic fields at its edges, as can be seen by comparing Figs. 1(b) and 1(c). At $\mu_0 H_{z,ext} = 1.2$ mT, we observe the nucleation of a dark ring, indicated by the black arrow in Fig. 1(d), in close vicinity to the outer edge of the sample. Upon increasing the external magnetic field, the position of the dark ring shifts toward the inner edge of the sample, as shown in Fig. 1(e). At $\mu_0 H_{z,ext} = 1.8$ mT the dark ring is close to the inner edge of the sample and, above this field value, its position becomes field independent.

III. SIMULATIONS AND DISCUSSION

To better understand the experimental results we performed numerical simulations inspired by those of Brandt,²⁴ in which the magnetic field profiles as well as the current distribution in the sample are calculated numerically. The details of the calculation are given in Appendix but they come down to the following. When an external magnetic field is applied to the superconducting ring, a shielding current starts to flow in the superconductor, which in turn generates a magnetic field. This magnetic field magnetizes the magnetic layer, which in turn changes the magnetic field experienced by the superconductor [see Fig. 2(f)]. The self-consistent solution to this problem is found by casting it in a time-dependent form in which the time derivative of the shielding current (the current flowing in the superconductor) is a function of the time derivative of the external field, the time derivative of the field generated by the magnetic ring (see below) and the shielding current itself. In this way, there is a direct (but rather complicated) relation between the shielding current and its time derivative. From this, the shielding current is calculated iteratively. This iterative calculation yields the current in the ring as a function of increasing external field, in direct correspondence to the experiment. The superconducting layer is subdivided into a number of concentric subrings, a procedure that enables the calculation of the whole *current distribution* in the layer. From this, one may easily calculate the magnetic field due to the superconductor and hence the magnetization of the magnetic material. For simplicity, the magnetic ring is modeled as a susceptible material with high in-plane susceptibility and zero susceptibility in the z direction. This is justified because immediately above the superconductor the in-plane component of the total field (external+shielding field of the superconductor) is much larger than its z component.²⁵ In the simulation, the superconductor and the magnetic material are allowed to adapt to each other's presence. Hence, in the main iteration loop there is a subloop of "relaxant" steps, which changes the values of the currents I flowing in the superconductor and the (z component of the) magnetic field due to the ferromagnetic layer, $H_{z,F}$ to make them mutually consistent before the external field is increased. A practical problem in the simulation is the small thickness of the ferromagnet in comparison with the diameter of the ring, which makes it difficult to choose an appropriate (fine enough) grid close to

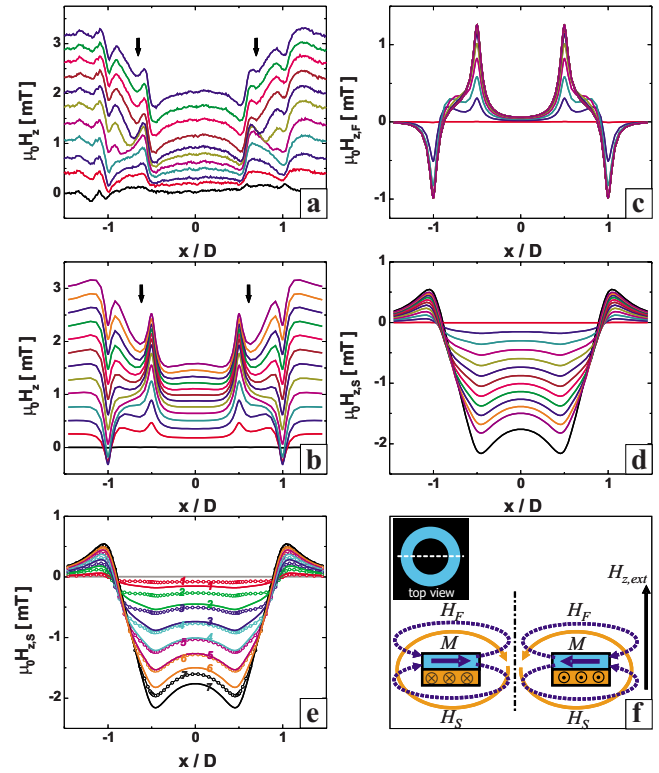


FIG. 2. (Color online) Profiles of the z component of the magnetic field in the indicator layer at the upper surface of the hybrid sample. Shown are the full experimental (a) and simulated (b) profiles. The experimental profiles were taken along the white dotted line shown in the inset of (f). The arrows point to the position of the dark ring [cf. the black arrow in Figs. 1(c) and 1(d)]. In (c) the contribution due to the magnetic layer is shown separately while in (d) the contribution due to the superconducting layer is shown. In (e) we show simulated profiles due to the superconducting layer for samples with (open symbols) and without (continuous lines) the presence of the magnetic layer. The profiles corresponding to the same external field are labeled with the same numbers. Figure 2(f) is a schematic view of the cross section of the composite sample. The dash-dotted line is the axis of rotational symmetry, which coincides with the z axis. Due to the applied magnetic field, which is parallel to the z axis, shielding currents start to flow in the superconductor (lower layer, orange) as indicated by the symbols \otimes and \odot . Due to these shielding currents, a magnetic field H_S is generated (indicated by the orange curved line). This field induces a radial magnetization M in the magnetic ring (upper layer, blue), which creates a field H_F in the space around the magnetic ring (indicated by the blue dotted curved line), which in turn changes the local field at the position of the superconductor.

the edges. To alleviate this problem, the thickness of the magnetic film is taken much larger than its corresponding value in reality while making sure that its maximum magnetic moment is equal to the known maximum magnetic moment of the real a -Gd₁₉Ni₈₁-layer.

The simulation allows us to separate the contributions from the superconductor and the ferromagnet, as we will now discuss. Due to the applied magnetic field, shielding currents start to flow in the superconductor, indicated in Fig. 2(f) by the \otimes and \odot symbols in the lower orange ring. These shielding currents generate the self-field of the supercon-

ductor, indicated by the orange arrows. This self-field is parallel to the applied field at the outer edge of the ring and antiparallel at its inner edge.²³ Hence, the z component of the local field at the outer edge of the ring is enhanced while it is reduced at its inner edge. The corresponding simulated field pattern is given in Fig. 2(d). It would lead to a bright outer edge of the ring and a dark inner edge, opposite to the situation observed for the hybrid ring. In the hybrid sample, the self-field of the superconductor magnetizes the ferromagnet (blue layer) in the radial direction (thick blue arrows). The resulting stray field of the ferromagnet is indicated by the dotted blue arrows. Our magneto-optical observations are made in a plane immediately above the ferromagnetic layer. In that plane and at the outer edge of the ring, the z component of the stray field of the ferromagnet is antiparallel to the applied field and the stray field of the superconductor. This leads to a very small total field at the outer edge, which thus appears as dark in the magneto-optical image. At the inner edge, the z component of the stray field of the ferromagnet enhances the externally applied field (and is antiparallel to the self-field of the superconductor). As a result there is a field enhancement at the inner edge, which thus appears as bright, see Fig. 1. This picture is corroborated by the result of our simulations, which show [Fig. 2(c)] that the ferromagnetic layer generates a negative field at the outer edge and positive field at the inner edge (note the applied field is positive). The sum of the stray fields of ferromagnet and superconductor, together with the applied field, make up the total field. The total z component of the field at the position of our measurement (at the magneto-optic indicator) is shown in Fig. 2(b). Due to the field enhancement of the ferromagnet, its profile is dominant, leading to the “inverted” behavior as compared to a pure superconductor. However, the contribution from the superconductor is still significant and the combination of both leads to the observed black ring [indicated by the arrows in Figs. 1(c), 1(d), 2(a), and 2(b)].

With increasing magnitude of $H_{z,ext}$, the in-plane magnetization of the sample increases, which is reflected by the increase in contrast, Fig. 1(b), and the enhancement of the height difference of the magnetic field profiles at the inner and outer edges of the ring, Figs. 2(a) and 2(b). This is associated with a gradual rotation of the spins in the a-Gd₁₉Ni₈₁ layer away from an initial tangential to a final radial direction, leading to the increased height difference between inner and outer edge in Fig. 2(c). This behavior is made possible in view of the virtual absence of domain-wall pinning in the amorphous a-Gd₁₉Ni₈₁ layer. Consistent with this picture, to obtain agreement between experiment and simulation, it was necessary to assume a radial saturation magnetization of the a-Gd₁₉Ni₈₁ layer that corresponds to the situation where all the spins point in the radial direction. Although the in-plane saturation magnetization of the 75-nm-thick a-Gd₁₉Ni₈₁ layer corresponds to 1 T, the z component of the stray field generated by this layer is only a few mT when averaged over the thickness (4 μ m) of the indicator used for the magneto-optical determination of H_z . Clearly, the results of the simulation, shown in Fig. 2(b), nicely reproduce the experimental features of the magnetic field distribution at the surface of the sample shown in Fig. 2(a).

It is important to note that the field profiles above T_c are completely different (above T_c we observe magneto-optically only a weak outline of the ring). This implies, that the stray fields we observe from the ferromagnetic layer are indeed due to a change in its (direction of) magnetization, induced by the self-field of the superconductor.

The evolution of the magnetic field profiles due the superconducting layer only of our composite sample, shown in Fig. 2(d) is *qualitatively* not different from the one observed in the experiment for a pure superconducting ring of Ref. 23. Nor from the simulated profiles of a bare superconductor, shown for comparison in Fig. 2(e). The bold lines correspond to the bare superconductor and the open symbols to the hybrid sample. The profiles obtained for the same external field are labeled with the same number. However, it can be clearly seen that there is a *quantitative* difference: the self-field of the superconducting layer in the hybrid structure is systematically smaller than the field in the bare superconducting layer. This implies that the currents which are flowing in the superconducting layer of the hybrid ring are smaller. Since proximity effects, that may lead in practice to the decrease of the critical current density, are not taken into account in our simulation, the observed difference in the calculated profiles can be fully attributed to the shielding provided by the magnetic layer. Due to its large susceptibility and virtual absence of coercivity, the magnetic layer enhances the shielding due to the shielding currents in the superconductor. As a consequence these shielding currents *are* reduced. Alternatively, for a fixed J_c , the maximum applied field that can be shielded is enhanced.

In conclusion, the presence of the magnetic layer reduces the shielding currents flowing in the superconducting ring and hardens the sample against the effects of external magnetic fields.

ACKNOWLEDGMENTS

The authors are grateful to E. H. Brandt and K. Heeck for suggestions. This work was supported by FOM (Stichting voor Fundamenteel Onderzoek der Materie) which is financially supported by NWO (Nederlandse Organisatie voor Wetenschappelijk Onderzoek).

APPENDIX: SIMULATION DETAILS

In the presence of an externally applied magnetic field, $H_{z,ext}\hat{z}$, a shielding current distribution is flowing in the superconducting layer. In spherical coordinates (r , θ , and φ), the vector potential for a single loop of current I and radius a is given by²⁶

$$A_\varphi(r, \theta) = \frac{\mu_0}{4\pi} I a \int_0^{2\pi} \frac{\cos \varphi d\varphi}{(a^2 + r^2 - 2ar \sin \theta \cos \varphi)^{1/2}}. \quad (\text{A1})$$

Due to symmetry all other components of the vector potential are zero. For a thin ring of inner radius a_1 , outer radius a_2 and in the plane of the sample ($\theta = \pi/2$), the above equation becomes

$$A_\varphi(r) = \frac{\mu_0}{4\pi} \int_{a_1}^{a_2} I(a) a \int_0^{2\pi} \frac{\cos \varphi d\varphi}{(a^2 + r^2 - 2ar \cos \varphi)^{1/2}} da. \quad (\text{A2})$$

By discretizing the radial position a in the plane of the ring with a grid of discrete elements Δa , Eq. (A2) can be written as

$$A(r) = \frac{\mu_0}{4\pi} \sum_{p=a_1}^{a_2} I(p) Q(p, r) \quad (\text{A3})$$

which has $[(a_2 - a_1)/\Delta a]$ terms.²⁷

$I(p)$ is the current spanning over the width Δa of each grid element and the kernel Q is defined as

$$Q = p \int_0^{2\pi} \frac{\cos \varphi d\varphi}{(p^2 + r^2 - 2pr \cos \varphi)^{1/2}}. \quad (\text{A4})$$

In the absence of the magnetic material, the total vector field A_{total} is the result of two contributions: the vector field due to the externally applied magnetic field, $A_{\varphi, ext}$ and the vector field due to the current flowing in the ring $A_{\varphi, ring}$. From $\vec{B} = \nabla \times \vec{A}$ expressed in cylindrical coordinates, the vector potential corresponding to the external magnetic field $H_{z, ext} \hat{z}$ can be written as $A_{\varphi, ext} = \mu_0 \frac{r}{2} H_{z, ext}$, hence using Eq. (A3),

$$\begin{aligned} A_{\varphi, total}(r) &= A_{\varphi, ring}(r) + A_{\varphi, ext}(r) \\ &= \frac{\mu_0}{4\pi} \sum_{p=a_1}^{a_2} I(p) Q(p, r) + \mu_0 \frac{r}{2} H_{z, ext} \end{aligned} \quad (\text{A5})$$

or in matrix notation,

$$\vec{A}_{total} = \frac{\mu_0}{4\pi} \vec{Q} \cdot \vec{I} + \mu_0 \frac{r}{2} H_{z, ext}. \quad (\text{A6})$$

By taking the time derivative and rearranging the terms of the above equation we obtain

$$\frac{\mu_0}{4\pi} \dot{\vec{I}} = \vec{Q}^{-1} \left(\dot{\vec{A}}_{total} - \mu_0 \frac{r}{2} \dot{H}_{z, ext} \right). \quad (\text{A7})$$

For this cylindrical geometry $\dot{\vec{A}}_{\varphi, total} = -E$ and $E = \rho j$, where ρ is the resistivity and $j = \frac{I}{d\Delta a}$ with d is the thickness of the sample. To proceed, we need to know ρ . Due to the geometry, with the external field applied perpendicular to our thin-film superconductor, there is a large demagnetization factor leading to a negligibly small penetration field (“effective H_{c1} ”). Hence we assume that the superconductor is always in the mixed state. We use for the resistivity in the mixed state $\rho = \rho_0 (j/j_c)^{n-1}$, with $n = U_0/kT \gg 1$ the creep exponent.²⁴ We note that the resistivity (through ρ_0) and critical current (through j_c) are taken to be field independent. The combination of ρ_0 , n , and j_c was taken such that the current in the superconductor corresponds to that in the experiment. Using a thus defined ρ , Eq. (A7) can be rewritten as

$$\dot{\vec{I}} = \frac{4\pi}{\mu_0} \vec{Q}^{-1} \left(-R_0 |\vec{I}|^n \vec{I} - \mu_0 \frac{r}{2} \dot{H}_{z, ext} \right). \quad (\text{A8})$$

This is the main equation used for our simulation. The inverse of the kernel Q is used only implicitly, as detailed in Ref. 28. Equation (A8) is iterated numerically to obtain I from $I(t + \Delta t) = I(t) + \dot{I} \Delta t$, starting from $I = 0$.

For the present simulation we take $H_{z, ext}$ as linearly increasing with time.

Once \vec{I} is known, the algorithm proceeds at each time step with the calculation of the magnetic field generated by this current, at any position \vec{x} , using for each subring with width Δa and radius a ,

$$\begin{aligned} \vec{H}_S \begin{pmatrix} x \\ y \\ z \end{pmatrix} &= \frac{I}{4\pi} \int \frac{d\vec{\ell} \times \vec{s}}{|\vec{s}|^3} \\ &= \frac{I}{4\pi} \int_0^{2\pi} \frac{\begin{pmatrix} x - a \cos \phi \\ y - a \sin \phi \\ z \end{pmatrix} \times \begin{pmatrix} a \sin \phi d\phi \\ -a \cos \phi d\phi \\ 0 \end{pmatrix}}{\left| \begin{pmatrix} x - a \cos \phi \\ y - a \sin \phi \\ z \end{pmatrix} \right|^3}. \end{aligned} \quad (\text{A9})$$

Due to the cylindrical symmetry of the sample, the field distributions in all planes containing the z axis are the same. Hence, we may use the distribution in the $y=0$ plane to obtain, in the coordinates (r, z) , the following field for the whole ring with current distribution $I(p)$,

$$\vec{H}_S(r, z) = \sum_{p=a_1}^{a_2} I(p) \int_0^\pi \frac{2}{4\pi} \frac{\begin{bmatrix} zp \cos \varphi d\varphi \\ (p^2 - rp \cos \varphi) d\varphi \end{bmatrix}}{(r^2 - 2rp \cos \varphi + p^2 + z^2)^{3/2}}. \quad (\text{A10})$$

The in-plane radial magnetic field $H_r = H_{r, S}$ induces a magnetization \vec{M} in the magnetic layer. In our simulation, this magnetization is taken to be purely radial (see discussion below) and will be denoted by M_r . To describe the susceptibility and its saturation we use $M_r = M_0 \tanh(H_r/H_0)$, with M_0 and H_0 appropriate constants. The resulting magnetization can be completely described by the currents flowing in the bulk, $\vec{J}_b = \nabla \times \vec{M}$, and at the surface, $\vec{K} = \vec{M} \times \hat{n}$, of the magnetic layer.²⁹ In our simulation we only consider the effects of the surface currents. This choice is justified as follows: in cylindrical coordinates we have

$$\begin{aligned} \vec{J}_b &= \vec{\nabla} \times \vec{M} = \left[\frac{1}{r} \frac{\partial M_z}{\partial \varphi} - \frac{\partial M_\varphi}{\partial z} \right] \hat{r} + \left[\frac{\partial M_r}{\partial z} - \frac{\partial M_z}{\partial r} \right] \hat{\phi} \\ &\quad + \frac{1}{r} \left[\frac{\partial(rM_\phi)}{\partial r} - \frac{\partial M_r}{\partial \phi} \right] \hat{z}. \end{aligned} \quad (\text{A11})$$

For a thin layer of magnetic material, which is the case in our experiment, the magnetization \vec{M} is independent of z , leading to the vanishing of the $\frac{\partial}{\partial z}$ terms. Taking into account only the

in-plane magnetization leads to a vanishing of M_z . Due to the circular symmetry M_ϕ is zero and $\frac{\partial M_r}{\partial \phi} = 0$. Hence, under these assumptions, the contribution of the bulk currents to the overall magnetization is zero. Knowing the magnetization induced by the field H_r , the surface current can be easily determined from $\vec{K} = \vec{M} \times \hat{n} = [\chi(\vec{H}_{z,ext} + \vec{H}_S)] \times \hat{n}$. Analogous to Eq. (A10), $\vec{H}_F = \chi(\vec{H}_{z,ext} + \vec{H}_S) = \vec{S} \cdot \vec{K}$, where \vec{H}_F is the field inside the magnetic layer and \vec{S} is the integral in Eq. (A10). The current needed to generate \vec{H}_F can be calculated from $\vec{K} = \vec{S}^{-1} \cdot \vec{H}_F$.

In the simulation, $H_{z,F}$ is calculated in an analogous way as the field due to the currents in the superconductor and added to the externally applied field $H_{z,ext}$ experienced by the superconducting layer. The new value of I is evaluated self-consistently using Eq. (A8), modified to include the contribution of the magnetic material to the vector potential, $A_{\phi,ext} = \mu_0 \frac{r}{2} H_{z,ext} + A_{\phi,F}$. It is not necessary to consider the effect of the radial component of \vec{H}_F on the superconductor because of our thin-film geometry and the small demagnetization factor of the superconducting film associated to $H_{r,F}$.

-
- ¹A. I. Buzdin, Rev. Mod. Phys. **77**, 935 (2005).
²F. S. Bergeret, A. F. Volkov, and K. B. Evetov, Rev. Mod. Phys. **77**, 1321 (2005).
³A. Yu. Rusanov, M. Hesselberth, J. Aarts, and A. I. Buzdin, Phys. Rev. Lett. **93**, 057002 (2004).
⁴T. W. Clinton and M. Johnson, Appl. Phys. Lett. **76**, 2116 (2000).
⁵R. Steiner and P. Ziemann, Phys. Rev. B **74**, 094504 (2006).
⁶D. Stamopoulos, E. Manios, and M. Pissas, Phys. Rev. B **75**, 184504 (2007).
⁷Z. Yang, M. Lange, A. P. Volodin, R. Szymczak, and V. V. Moshchalkov, Nature Mater. **3**, 794 (2004).
⁸W. Gillijns, A. Yu. Aladyshev, M. Lange, M. J. Van Bael, and V. V. Moshchalkov, Phys. Rev. Lett. **95**, 227003 (2005).
⁹Yu. A. Genenko, A. Usoskin, and H. C. Freyhardt, Phys. Rev. Lett. **83**, 3045 (1999).
¹⁰Yu. A. Genenko, H. Rauh, and A. Snezhko, Physica C **372-376**, 1389 (2002).
¹¹A. V. Pan, S. Zhou, H. Liu, and S. Dou, Supercond. Sci. Technol. **16**, L33 (2003).
¹²H. Jarzina, Ch. Joos, and H. C. Freyhardt, J. Appl. Phys. **91**, 3775 (2002).
¹³V. V. Yurchenko, D. V. Shantsev, Y. M. Galperin, A. K. M. Alamgir, Z. Han, and T. H. Johansen, Physica C **460-462**, 803 (2007).
¹⁴S. V. Dubonos, A. K. Geim, K. S. Novoselov, and I. V. Grigorieva, Phys. Rev. B **65**, 220513 (2002).
¹⁵H.-Y. Wu, J. Ni, J.-W. Cai, Z.-H. Cheng, and Y. Sun, Phys. Rev. B **76**, 024416 (2007).
¹⁶C. Monton, F. de la Cruz, and J. Guimpel, Phys. Rev. B **77**, 104521 (2008).
¹⁷A. Yu. Rusanov, M. B. S. Hesselberth, and J. Aarts, Phys. Rev. B **70**, 024510 (2004).
¹⁸C. Bell, S. Turşucu, and J. Aarts, Phys. Rev. B **74**, 214520 (2006).
¹⁹E. H. Brandt, Phys. Rev. B **49**, 9024 (1994).
²⁰M. R. Koblischka and R. J. Wijngaarden, Supercond. Sci. Technol. **8**, 199 (1995).
²¹R. J. Wijngaarden, K. Heeck, M. Welling, R. Limburg, M. Pannetier, K. van Zetten, V. L. G. Roorda, and A. R. Voorwinden, Rev. Sci. Instrum. **72**, 2661 (2001).
²²R. J. Wijngaarden, C. M. Aegerter, M. S. Welling, and K. Heeck, in *Magneto-optical imaging*, NATO Science Series: II: Mathematics, Physics and Chemistry Vol. 142, edited by T. H. Johansen and D. V. Shantsev (Kluwer Academic, Dordrecht 2003), p. 61.
²³M. Pannetier, F. C. Klaassen, R. J. Wijngaarden, M. Welling, K. Heeck, J. M. Huijbregtse, B. Dam, and R. Griessen, Phys. Rev. B **64**, 144505 (2001).
²⁴E. H. Brandt, Phys. Rev. B **55**, 14513 (1997).
²⁵A. Forkl, H. U. Habermeier, B. Leibold, T. Dragon, and H. Krohnmüller, Physica C **180**, 155 (1991).
²⁶J. D. Jackson, *Classical Electrodynamics*, 2nd ed. (Wiley, New York, 1975), p. 173.
²⁷In the simulation we use a nonequidistant grid with appropriate weights, as defined by E. H. Brandt, Phys. Rev. B **58**, 6506 (1998); and E. H. Brandt and J. R. Clem, Phys. Rev. B **69**, 184509 (2004). We use the interpolation scheme of the latter paper, however with the correct expression $r(u) = a + (b - a)(10u^3 - 15u^4 + 6u^5)$. For didactic purposes, we omit the weights in the equations, which is equivalent to the use of an equidistant grid with period Δa .
²⁸R. J. Wijngaarden, H. J. W. Spoelder, R. Surdeanu, and R. Griessen, Phys. Rev. B **54**, 6742 (1996).
²⁹D. J. Griffiths, *Introduction to Electrodynamics*, 3rd ed. (Wiley, New York, 1999), p. 264.